



# Nickel-grafted TUD-1 mesoporous catalysts for carbon dioxide reforming of methane

Xian-Yang Quek<sup>1,2</sup>, Dapeng Liu<sup>1</sup>, Wei Ni Evelyn Cheo, Hong Wang, Yuan Chen, Yanhui Yang<sup>\*</sup>

School of Chemical and Biomedical Engineering, Nanyang Technological University, Singapore 637459, Singapore

## ARTICLE INFO

### Article history:

Received 4 September 2009

Received in revised form 19 December 2009

Accepted 20 January 2010

Available online 25 January 2010

### Keywords:

TUD-1  
Nickel  
Grafting  
Dry reforming

## ABSTRACT

The nickel active sites were introduced into TUD-1 mesoporous molecular sieve via grafting, direct synthesis, and impregnation methods. These samples were characterized using powder X-ray diffraction, N<sub>2</sub> physisorption, H<sub>2</sub> temperature-programmed reduction, H<sub>2</sub> chemisorption, TG/DTA, temperature-programmed hydrogenation, Raman spectra and transmission electron microscope to give the insight of physicochemical properties. Catalytic tests probed by the carbon dioxide reforming of methane revealed that Ni-grafted TUD-1 exhibited the highest catalytic activity and long-term stability among these catalysts. Further studies implied catalytic activity, stability and carbon formation were highly sensitive to the metallic nickel particle size which was significantly affected by the introduction method of Ni active sites. Strong anchoring effect inherent to the grafting method was suggested to be the underlying reason for the small Ni particle size and improved catalytic performance.

© 2010 Elsevier B.V. All rights reserved.

## 1. Introduction

Due to its relatively low cost and availability, the application of ferrous metal (Fe, Co and Ni) as catalytically active component is preferred over noble metals. Nickel has attracted wide attention because of its high catalytic performance in various processes of considerable importance in chemical industry, including hydro-desulfurization [1], selective oxidation of hydrogen sulfide [2], carbon dioxide and steam reforming [3,4]. Methane dry reforming, which can efficiently transform two most abundant greenhouse gases (carbon dioxide and methane) into synthesis gas, has generated interest from both industrial and environmental viewpoints. The use of nickel catalysts for the methane dry reforming was investigated on various carriers such as SiO<sub>2</sub> [5], Al<sub>2</sub>O<sub>3</sub> [6], ZrO<sub>2</sub> [7], and zeolite [8]. However there are several issues associated with the rapid deactivation of supported nickel catalyst including: (1) sintering of catalyst at high reaction temperature and (2) catalyst deactivation due to carbon deposition [5,9–11].

Since the discovery of M41S silicates by Mobil scientists, mesoporous silica materials have drawn increasingly growing attention in the field of heterogeneous catalysis research due to their well defined tunable pore structure, high specific surface area and flexible heteroatom compositions [12,13]. The prominence of

M41S family silicate material has subsequently motivated the development of other mesoporous silicates such as SBA-15 [14] and more recently TUD-1 [15]. To develop a stable and effective methane dry reforming catalyst, an appropriate combination of nickel active sites and mesoporous silicate support is expected to be promising [16–19]. Numerous studies on using SBA-15 as catalyst supports have been reported due to its advantage of thick pore wall and high thermal stability, hence favoring the reactions occurring at high temperatures [17–20]. It was observed that the mesoporous structure of SBA-15 was appreciably retained even after reaction at 800 °C for 710 h for methane reforming with CO<sub>2</sub> [20]. By employing Ni/SBA-15/FeCrAl monolithic catalysts, the catalytic activity and stability were further improved [21].

The method of introducing active component plays an important role in controlling the activity and the stability of catalyst. For the studies on methane dry reforming using supported nickel, impregnation on various carriers was the most widely employed method [16,18–23]. Recently, our group has reported that nickel directly incorporated MCM-41 (Ni-MCM-41) was more stable and effective for the carbon dioxide reforming of methane compared to the impregnated catalyst [4]. Grafting is another common method to prepare supported catalysts [24–26]. Du et al. have reported the highly dispersed vanadium active sites on SBA-15 by grafting method [25]. It was suggested that the isolated vanadium sites resulted in the high selectivity in the partial oxidation of methanol to formaldehyde. To our knowledge, the preparation of Ni-grafted mesoporous silicate is rare, the indirect route via the reaction of nickel sulfate with organoamine-functionalized MCM-41 was reported as a novel sorbent material to remove Naproxen contaminant [26].

<sup>\*</sup> Corresponding author at: 62 Nanyang Drive, N1.2-B1-18, Singapore 637459, Singapore. Tel.: +65 6316 8940; fax: +65 6794 7553.

E-mail address: [yhyang@ntu.edu.sg](mailto:yhyang@ntu.edu.sg) (Y. Yang).

<sup>1</sup> These authors equally contributed to this work.

<sup>2</sup> Current address: Schuit Institute of Catalysis, Eindhoven University of Technology, Netherlands.

In this study, nickel as the active component supported on a novel thick-wall mesoporous silicate TUD-1 for dry reforming of methane is reported. TUD-1 material can be readily synthesized with a surfactant-free method, which is environmentally friendly and cost-effective [15]. Particularly, its high thermal stability, three-dimensional sponge-like silicate framework with high surface area and substrate accessibility make it advantageous over other microporous and mesoporous materials [27]. Different methods of introducing nickel to TUD-1 support, namely direct synthesis, conventional impregnation and post-synthesis grafting, were employed and the catalytic performance and stability of synthesized catalysts were evaluated in carbon dioxide reforming of methane.

## 2. Experimental

### 2.1. Catalyst preparation

TUD-1 mesoporous silicate was synthesized following the method reported by Jansen et al. [15]. Ni-grafted TUD-1 catalyst (denoted by Ni-GRF) was prepared by adding 2 g of TUD-1 to 120 ml of toluene (anhydrous, 99.8% Sigma-Aldrich) and refluxing at 110 °C for 5 h under N<sub>2</sub> flow. Subsequently, 0.51 g nickel(II) acetylacetonate (95%, Aldrich) pre-dissolved in toluene at 80 °C was added to the above-mentioned suspension and refluxed at 110 °C for another 12 h under N<sub>2</sub> flow. The mixture was then filtered, washed with toluene and dried at 80 °C. Ni-TUD-1 catalyst prepared by direct incorporation (denoted by Ni-DHT) was synthesized by a modified method reported elsewhere [15]. 0.75 g of nickel(II) nitrate hexahydrate (Ni(NO<sub>3</sub>)<sub>2</sub>·6H<sub>2</sub>O, 99%, Acros) dissolved in deionized water was added to tetraethyl orthosilicate (TEOS) prior to adding triethanolamine solution. Nickel impregnated TUD-1 catalyst (denoted as Ni-IMP) was prepared via the incipient impregnation using Ni(NO<sub>3</sub>)<sub>2</sub> as a nickel precursor. All prepared nickel catalysts were calcined in air at 600 °C for 10 h. Due to the partial loss of nickel precursor during the synthesis and post-synthesis grafting, the nickel loading was measured by ICP analysis.

### 2.2. Catalyst characterization

Powder X-ray diffraction (XRD) patterns were recorded on a Bruker Advance 8 diffractometer (under ambient conditions) using filtered Cu K $\alpha$  radiation ( $\lambda$  = 0.15406 nm) operated at 40 kV and 40 mA. Diffraction data were collected from  $2\theta$  of 0.5–8° (resolution of 0.02°) and 5–70° (resolution of 0.05°), respectively. Nitrogen physisorption isotherms were measured at –196 °C with a static volumetric instrument Autosorb-6B (Quanta Chrome). Prior to measurements, the samples were degassed at 200 °C for 12 h under high vacuum. The specific surface areas were calculated using the BET method [28] and the pore size distributions were estimated by the BJH method [29] using the desorption branch.

In situ FT-IR spectra were measured using a PerkinElmer Spectrum One at a resolution of 2 cm<sup>–1</sup> and accumulation of 20 scans. Prior to each measurement, the self-supporting sample disc was heated from room temperature to 120 °C and maintained for 30 min under helium flow. Laser-Raman spectra were recorded in the range of 1000–2000 cm<sup>–1</sup> using a 633 nm laser excitation on a Renishaw inVia Raman imaging microscope spectrometer with a Nd:YAG laser source under ambient condition.

The reducibility of the catalyst was studied by hydrogen temperature-programmed reduction (TPR) on Autosorb-1C (Quantachrome) apparatus. Before reduction, the sample was pretreated under flowing air at 500 °C for 60 min. All TPR runs were performed using 5 vol.% H<sub>2</sub> in Ar with a heating rate of 8 °C/min from 90 to

800 °C. The consumption of hydrogen was monitored on-line with a thermal conductivity detector (TCD).

Hydrogen chemisorption was performed in a conventional static volume apparatus Autosorb-1C (Quantachrome). The sample was first dried under He at 250 °C for 2 h and reduced in pure H<sub>2</sub> at 750 °C for 2 h. The sample was evacuated at this temperature for 2 h, followed by cooling under vacuum to ambient temperature at which the H<sub>2</sub> adsorption was to be determined. The dispersion is calculated on the adsorbed amounts of hydrogen determined with this isotherm by extrapolation of the linear part to zero pressure.

Carbon formation was quantitatively analyzed on a PerkinElmer Pyris Diamond TG/DTA instrument under air atmosphere. The heating rate is 10 °C/min within a temperature range of 30–800 °C. Carbon species formed during the stability test were also characterized by temperature-programmed hydrogenation (TPH). The spent catalyst was purged in He at 50 °C for 1 h before subject to H<sub>2</sub>. Subsequently, the feed gas was switched to H<sub>2</sub> flow and the temperature was increased from 50 to 800 °C at 5 °C/min of ramping rate. The vent gas was monitored with a TCD. A cold acetone trap was set between the sample cell and detector to condense the produced moisture.

### 2.3. Catalytic reaction experiments

Catalytic activity tests were performed under atmospheric pressure in a continuous down-flow quartz fixed-bed reactor. Typically, 0.12 g of catalyst was loaded on quartz wool. Prior to each test, the catalyst was pretreated in situ at 750 °C for 2 h under H<sub>2</sub>. The feed stream had a constant volume ratio of CH<sub>4</sub>/CO<sub>2</sub>/2He for all experiments. The weight hourly space velocity (WHSV) of the reactant gas mixture was fixed at 50,000 mL/(h gCat) except for the experiments which examine the effect of WHSV. The catalytic activity was measured by heating at temperatures ranging from 500 to 800 °C followed by cooling from 800 to 500 °C in steps of 50 °C and maintained for 40 min at each temperature. For stability test experiments, the reaction temperature was kept constant at 750 °C for 72 h time on stream (TOS). The composition of products was analyzed using an on-line gas chromatograph (Agilent 6890) equipped with a Porapak Q column and a thermal conductivity detector (TCD). The conversions of CH<sub>4</sub> and CO<sub>2</sub>, the selectivity of H<sub>2</sub> and CO and the ratio of CO/H<sub>2</sub> were calculated according to the previous reported method [4].

## 3. Results and discussion

### 3.1. Catalyst characterization

Fig. 1a illustrates the low-angle XRD patterns for the calcined Ni supported on TUD-1 samples. A strong diffraction peak, observed at the vicinity of  $2\theta$  = 0.8° for all the samples, evidences the presence of mesostructured porosity [27], implying that different methods of supporting Ni do not disturb the mesostructure of TUD-1. All these three calcined samples show several high-angle diffraction peaks at  $2\theta$  = 37.1°, 43.3° and 62.8° (Fig. 1b), which indicates the formation of crystalline NiO after calcination. Weak diffraction peak intensity suggests the nature of highly dispersed NiO clusters on TUD-1 surface. The physical properties of the catalysts were tested by N<sub>2</sub> physisorption to complement XRD results. Fig. 1c shows that all isotherms exhibit a sharp step increase in nitrogen uptake at relative pressure ( $P/P_0$ ) of 0.5–0.8 with a type IV hysteresis, representing a typical mesostructured feature with large pore diameter. A summary of the surface area, pore volume, pore diameter is shown in Table 1. Direct incorporation of Ni into the silica framework (Ni-DHT sample) results in pore shrinkage and a larger specific surface compared to pure siliceous TUD-1. Introducing nickel via impregnation

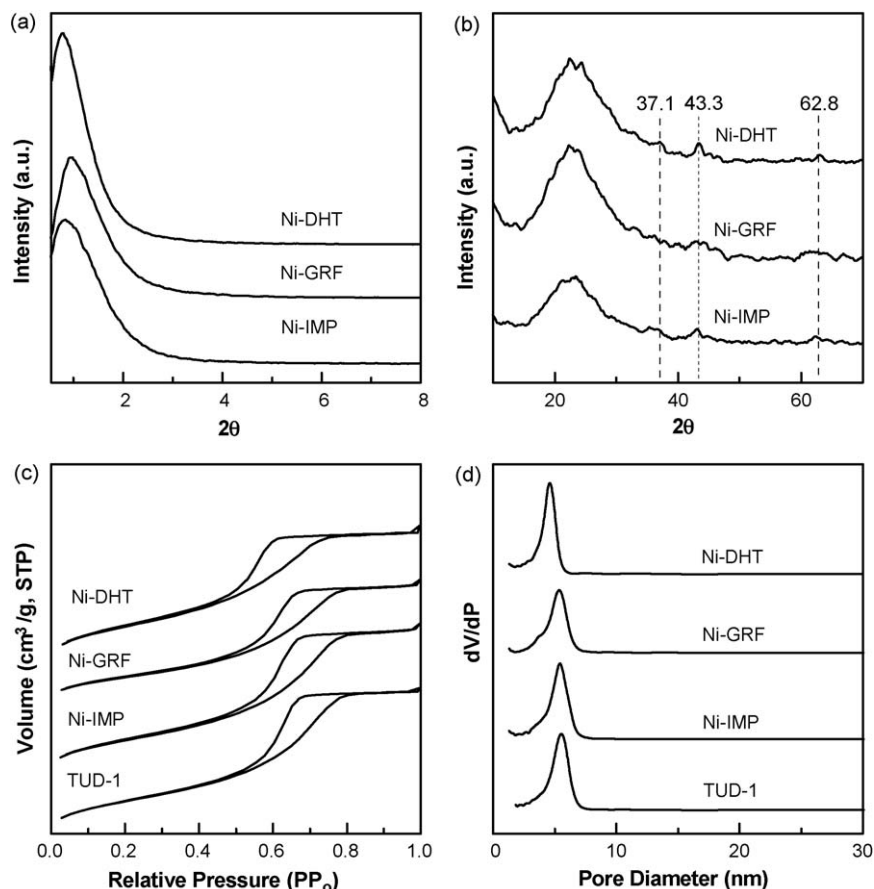


**Fig. 1.** (a) Low-angle XRD patterns, (b) high-angle XRD patterns, (c)  $N_2$  physisorption isotherms, and (d)  $N_2$  physisorption pore size distributions of Ni-containing TUD-1 catalysts.

remarkably decreases the specific surface area and the pore volume while the influence of post-grafting method on these two parameters is negligible. Moreover, the pore diameter is the same for both impregnated and grafted samples (Fig. 1d).

To quantitatively compare the density of surface terminal silanol groups (Si–OH), in situ IR experiments were tested for TUD-1, Ni-GRF and Ni-IMP catalysts and the results are shown in Fig. 2. The adsorption band observed from 3200 to 3800  $\text{cm}^{-1}$  is assignable to the stretching of Si–O–H bond [30]. Ni-GRF sample exhibits the lowest peak intensity, implying the successful substitution of the surface silanol group with nickel species. The similar result was also observed by Stucky et al., the silanol peak intensity declines with increasing metal loading, for Ti-grafted MCM-48 and SBA-15 [30]. Although there is a decrease in the intensity of silanol peak in Ni-IMP sample, the reduction in peak

intensity can be due to the blockage of terminal OH group by surface Ni species. Elemental analysis has confirmed that Ni-IMP sample has almost the same nickel loading compared to Ni-GRF. Hence it reveals that nickel has indeed been introduced onto TUD-1 via grafting which results in a significantly low surface OH density.

TPR profiles of the calcined Ni-containing TUD-1 are shown in Fig. 3. Three major reduction peaks at 345, 500, and 750  $^{\circ}\text{C}$  are observable for Ni-DHT sample along with a shoulder peak at 645  $^{\circ}\text{C}$ . The first peak at 345  $^{\circ}\text{C}$  resembles the reduction of bulk NiO species on Ni-DHT. Slightly higher reduction temperature compared to crystalline NiO may be attributed to the interaction between NiO nanoparticles and TUD-1 framework [31,32]. The main reduction at 500  $^{\circ}\text{C}$  and the shoulder peak at 645  $^{\circ}\text{C}$  may be caused by the reduction of nickel on the pore wall surface and in

**Table 1**  
Physiochemical properties of Ni-containing TUD-1 catalysts.

Sample	Ni loading <sup>a</sup> (%)	Surface area ( $\text{m}^2/\text{g}$ )	Pore diameter (nm)	Pore volume ( $\text{ml}/\text{g}$ )	Metal surface ( $\text{m}^2/\text{g}$ )	Dispersion <sup>b</sup> (%)	Ni cluster size <sup>c,d</sup> (nm)		
							D1	D2	D3
Ni-DHT	3.97	710	4.5	0.94	0.54	2.03	49.9	22.0	19.2
Ni-GRF	3.83	625	5.4	1.01	1.17	5.03	20.1	7.9	8.4
Ni-IMP	4.24	500	5.4	0.82	0.43	1.42	71.1	17.0	26.3
TUD-1	–	632	5.4	0.97	–	–	–	–	–

<sup>a</sup> The nickel content was measured by ICP test.

<sup>b</sup> Dispersion was calculated assuming  $H_{\text{ad}}/Ni_{\text{surf}} = 1$ .

<sup>c</sup> Metal particle shape was assumed to be spherical.

<sup>d</sup> D1 denotes Ni particle size of the reduced samples determined by  $H_2$  chemisorption, D2 and D3 are designated to Ni the particle size of spent catalysts determined by XRD and TEM, respectively.

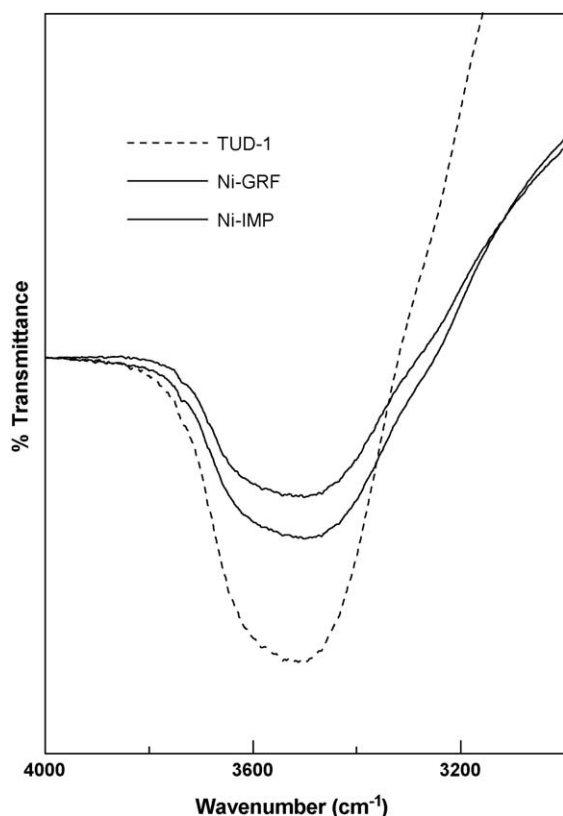


Fig. 2. In situ FT-IR spectra of Ni-containing TUD-1 catalysts.

the “bulk” of the silica framework, respectively [4]. Reduction peak at 750 °C is most likely due to the reduction of small amount of nickel species stronger interacting with support, probably in the form of nickel metasilicates [33,34]. For Ni-GRF sample, a sharp

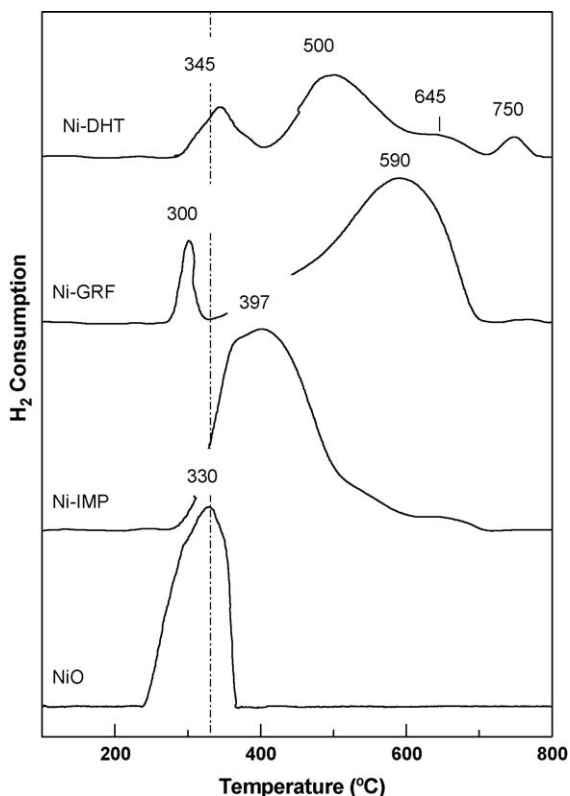


Fig. 3. H<sub>2</sub>-TPR of Ni-containing TUD-1 catalysts.

distinct and a broad wide peak can be observed at 300 and 590 °C, respectively. The first peak can be assigned to the reduction of NiO particles. A reasonable postulation for a lower temperature reduction of NiO species observed on Ni-GRF compared to crystalline NiO may be due to the formation of smaller NiO clusters which can be reduced at significantly lower temperature [35]. The second reduction peak at 590 °C can be attributed to the nickel species grafted onto the surface of TUD-1. Analogous to the previous report which showed that grafted vanadium species was reduced at higher temperature compared to the vanadium incorporated sample [36], it is convinced that grafted nickel species will also be reduced at higher temperature compared to the directly synthesized Ni-DHT sample. A single broad peak is observed for Ni-IMP sample, which resembles the reduction of NiO species on Ni-DHT sample and also crystalline NiO. The broad feature is probably related to the interaction between Ni and silica support with a quite heterogeneous nature [19].

Hydrogen chemisorption results for metal dispersion, metal surface area and particle size are summarized in Table 1. The nickel dispersions on all the samples are less than 10% after reduction. The active Ni metal surface area increases with the following sequence: Ni-IMP < Ni-DHT < Ni-GRF. Low active metal surface area and large Ni particles size observed on Ni-IMP can be attributed by substantial nucleation and rapid aggregation forming large Ni crystallites during the reduction. Weak interaction between TUD-1 and the surface Ni during reduction is suggested to be the main reason. On the contrary, high active metal surface area and small nickel particle size are observed on both Ni-GRF and Ni-DHT samples due to the strong anchoring effect of TUD-1 support. This anchoring restricts the migration of nickel clusters hence preventing the formation of large nickel particles. Grafted nickel species may provide a better catalyst synthesis method compared to framework incorporated nickel species as higher dispersion and smaller nickel particle size is observed on Ni-GRF sample.

### 3.2. Catalytic performance

Blank test using pure siliceous TUD-1 showed negligible non-catalytic gas phase reforming. The catalytic performances of various Ni-containing TUD-1 catalysts are shown in Fig. 4. The conversion is dependent on both the reaction temperature and the method of introducing Ni. An exponential increase in both CH<sub>4</sub> and CO<sub>2</sub> conversion with increasing temperature is observed for all these three catalysts. Ni-DHT exhibits the lowest initiation temperature followed by Ni-GRF and Ni-IMP (for instance, CH<sub>4</sub> conversions at 550 °C on Ni-DHT, Ni-GRF and Ni-IMP are 17.9%, 5.4% and 4.0%, respectively). Higher initiation temperature is observed for Ni-GRF in comparison to Ni-DHT despite the former sample having the highest active metal surface area and dispersion. This can be attributed to slightly lower Ni loading of 3.5% in Ni-GRF compared to 4.0% in Ni-DHT. A noticeable higher conversion is observed for CO<sub>2</sub> compared to CH<sub>4</sub>. The presence of reverse water gas shift (RWGS) reaction is suggested to be the main reason contributing to such higher CO<sub>2</sub> conversion.

H<sub>2</sub> selectivity and H<sub>2</sub>/CO ratio dependency on reaction temperature are shown in Fig. 4c and d, respectively. For all catalyst, H<sub>2</sub> selectivity increases exponentially with increasing temperature. This is in agreement with previous thermodynamics studies where high temperature favors the formation of H<sub>2</sub> through various reactions such as reforming, water gas shift reaction, carbon gasification and methane cracking [37]. Excess CO is observed (H<sub>2</sub>/CO ratio less than unity) over the entire range of temperature investigated. In particular, CO was found to be in greater excess at low temperature. This can be due to the occurrence of side reaction such as RWGS and methanation



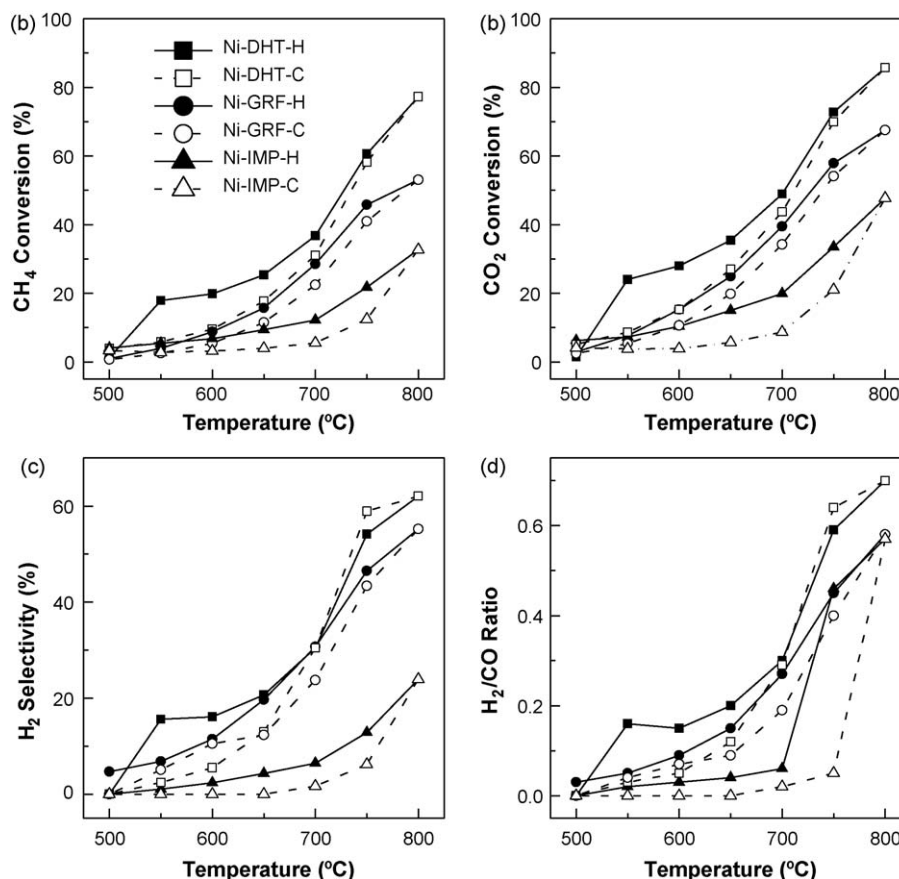


Fig. 4. Effect of temperature on the initial catalytic performance of Ni incorporated TUD-1 catalyst (H indicates heating from 500 to 800 °C, C indicates cooling from 800 to 500 °C).

reaction at low temperature which consumes H<sub>2</sub> [37]. Both Ni-DHT and Ni-GRF exhibit analogous H<sub>2</sub> selectivity while Ni-IMP shows obviously lower selectivity towards H<sub>2</sub>. Moreover, Ni-GRF exhibits noticeably lower H<sub>2</sub>/CO ratio compared to Ni-DHT, implying that less carbon is formed on Ni-DHT catalyst.

When the reaction temperature declines, a clear hysteresis loop of catalytic activity is formed for all these three samples (Fig. 4). Both Ni-DHT and Ni-GRF exhibit a narrow hysteresis loop while Ni-IMP presents a considerably wider hysteresis loop, suggesting that more severe sintering occurs on Ni-IMP during reaction and active nickel sites aggregate into large particles which are catalytically less active. Hence the catalytic performance for carbon dioxide reforming cannot be retained.

### 3.3. Stability of the catalysts

The catalytic stability of the prepared samples was investigated at 750 °C and the results are presented in Fig. 5. Both Ni-GRF and Ni-DHT are relatively stable at 750 °C for 72 h of TOS with Ni-GRF being more stable than Ni-DHT. The better anchoring effect of grafted nickel compared to framework incorporated nickel as mentioned in Section 3.1 can have contributed to the higher stability in Ni-GRF sample. Ni-IMP exhibits the poorest activity and stability, nearly no activity (in terms of CH<sub>4</sub> conversion) is observed during stability analysis on Ni-IMP sample after 5 h of TOS. As the conversions of two reactants are rather low and not sustained, deactivation via coke formation is unlikely. Therefore, the deactivation of Ni-IMP catalyst may be attributed to the metal sintering which is confirmed by the TEM observation later on (Fig. 10). From the results obtained, it can be assumed that nickel particle size is a crucial factor affecting activity of the catalyst. Based on our chemisorption and catalytic stability results, it is

suggested that the formation of smaller particle size is very beneficial for the carbon dioxide reforming of methane.

The H<sub>2</sub> selectivity and H<sub>2</sub>/CO ratio were tracked during the stability analysis (Fig. 5c and d). Both Ni-GRF and Ni-DHT catalysts are able to maintain high H<sub>2</sub> selectivity and H<sub>2</sub>/CO ratio during 72 h of TOS. Ni-IMP exhibit moderate H<sub>2</sub> selectivity and H<sub>2</sub>/CO ratio which deteriorate completely after 5 h. A slight decrease in H<sub>2</sub> selectivity and H<sub>2</sub>/CO ratio (stabilized after 25 h of TOS) is also observed on Ni-DHT. This decline can be due to the further nucleation of Ni particle at the reaction condition which is stabilized after 25 h of TOS. Although carbon deposition can be another reason for the observed decline in H<sub>2</sub> selectivity, no further decrease in the selectivity is observed despite both CH<sub>4</sub> and CO<sub>2</sub> conversion maintained above 50% and 60%, respectively.

### 3.4. Contact time effect

Ni-GRF was selected as the best catalyst to study the influence of contact time at 750 °C by varying the weighted hourly space velocity (WHSV). Variation of contact time was achieved by changing the total gas flow rate with the feed ratio fixed at CH<sub>4</sub>/CO<sub>2</sub>/2He. As shown in Fig. 6, both CH<sub>4</sub> and CO<sub>2</sub> conversions slightly decrease with increasing WHSV due to the decreased contact time. A more significant decrease in the both conversions was observed when WHSV increases from 40,000 to 50,000 h<sup>-1</sup> compared to the increase from 50,000 to 60,000 h<sup>-1</sup>. However, only trivial fluctuation of H<sub>2</sub>/CO ratio was observed with increasing WHSV.

### 3.5. Deactivation analysis

One major reason of dry reforming catalyst deactivation is that the catalyst is more susceptible to coke formation compared to

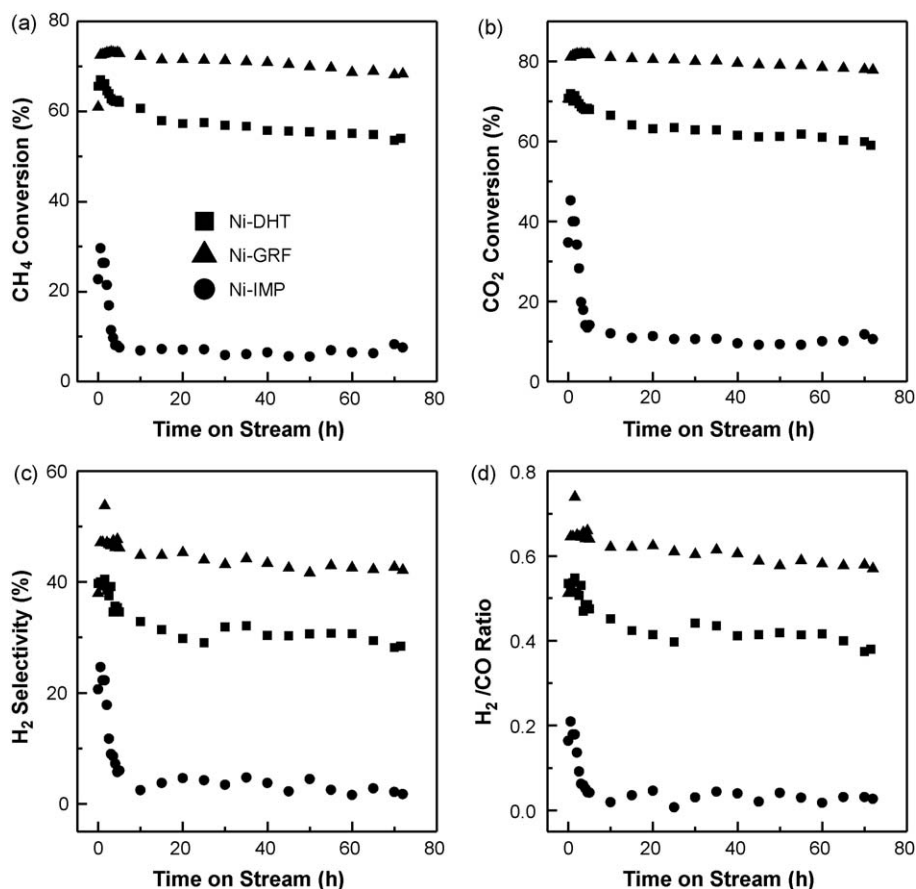


Fig. 5. Catalytic stability of Ni catalyst for the carbon dioxide reforming of methane at 750 °C for 72 h.

steam reforming catalyst in the absence of steam. Two main pathways lead to the carbon deposition in reforming:  $\text{CH}_4$  decomposition ( $\text{CH}_4 \rightarrow \text{C} + 2\text{H}_2$ ) and the CO disproportionation ( $2\text{CO} \rightarrow \text{C} + \text{CO}_2$ ), also known as the Boudouard reaction. The

deposited carbon can be diminished by carbon gasification ( $\text{H}_2\text{O} + \text{C} \rightarrow \text{CO} + \text{H}_2$ ), which is an endothermic reaction favored at high temperature [37]. In this study, the spent catalysts were characterized by XRD, DT/TGA and Raman to probe the impact of Ni incorporation method on the carbon deposition. High-angle XRD patterns (Fig. 7a) of the spent catalyst show the intensity of graphite peak increasing in the following sequence: Ni-IMP < Ni-DHT < Ni-GRF. No diffraction peak of graphite can be observed on the Ni-IMP catalyst, implying a negligible amount of carbon formation which may be due to the tremendously low activity. Ni-GRF catalyst with higher activity and stability is found to exhibit a higher intensity of graphite peak, suggesting more carbon is deposited on it compared to Ni-DHT catalyst.

Laser Raman, a sensitive technique used to probe the composition and nature of carbonaceous species present on the catalyst surface complements the results obtained by XRD, shown in Fig. 7b. Both a graphite-like band (G-band) at  $1580\text{ cm}^{-1}$  and a defect band (D-band) at  $1350\text{ cm}^{-1}$  exist for all the spent samples. G-band is attributed to the stretching of carbon  $\text{sp}^2$  bonds which is typically observed on graphite while D-band is contributed by the vibration of carbon atoms with dangling bonds in amorphous carbon network [4,38,39]. No Raman shift can be found for Ni-IMP while both Ni-DHT and Ni-GRF exhibit two Raman bands which are assigned to G-band and D-band, implying that both the amorphous carbon and graphite have been formed during the reaction.

The thermogravimetric analysis under oxidative atmosphere was performed in order to quantify the amount of carbon formed. Fig. 8 illustrates the TG/DTA profile for the spent catalyst after 72 h of TOS. Low-temperature weight loss at approximately  $100^\circ\text{C}$  corresponds to the removal of moisture. The weight loss of various samples was calculated based on the loss above  $110^\circ\text{C}$ . The weight loss percentage increases with the following sequence: Ni-IMP

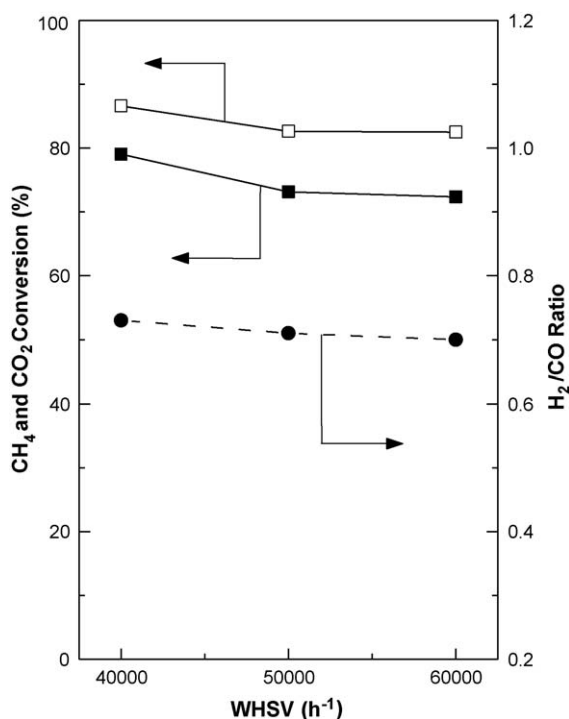


Fig. 6. Effect of WHSV on the initial catalytic performance of Ni-GRF catalyst.

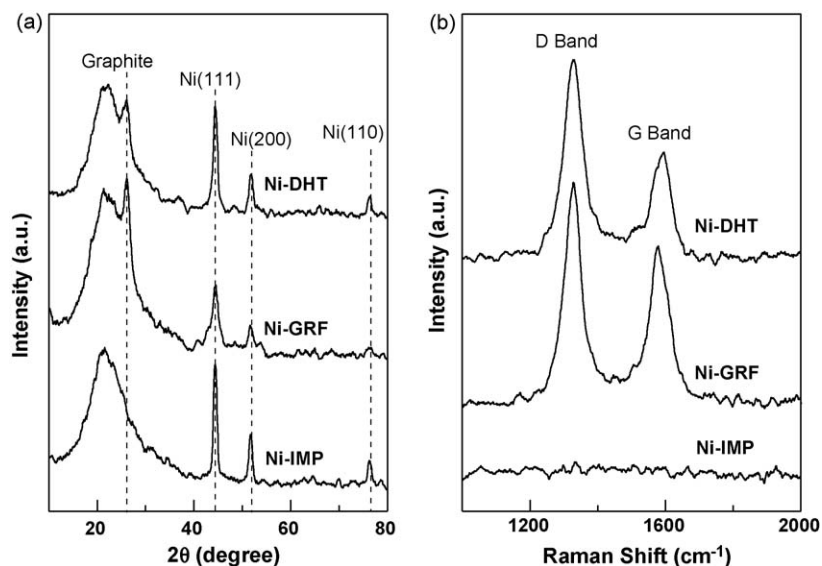


Fig. 7. (a) High-angle XRD patterns and (b) laser-Raman spectra for spent Ni-containing TUD-1 catalysts.

(0%) < Ni-DHT (11.1%) < Ni-GRF (15.5%). It is well known that higher temperature is required to oxidize the inert carbon component compared to the reactive carbon. Hence, based on the TGA profile, it can be concluded that the carbon formed on Ni-DHT and Ni-GRF are predominantly inert species since most of the deposited carbon oxidizes at temperature above 600 °C. Negligible amount of carbon is detected on Ni-IMP, which coincides with the observations of XRD and laser Raman. Trace weight gain is observed above 500 °C for the Ni-IMP sample which may be attributed to the oxidation of reduced Ni species on the catalyst.

The TPH profiles of Ni-containing catalysts after stability tests are shown in Fig. 9a. Three hydrogenation peaks were identified for the spent Ni-DHT catalyst at around 506, 573, 842 °C for  $\alpha$ -carbon,  $\beta$ -carbon, and  $\gamma$ -carbon, respectively. Considering the inertness of carbon species increases with the hydrogenation temperature, the reactivity of these carbon species decreases as follows:  $\alpha$ -carbon >  $\beta$ -carbon >  $\gamma$ -carbon. Over the spent Ni-GRF catalyst, only one broad peak centered around 576 °C is clearly observed, which corresponds to the  $\beta$ -carbon with moderate reactivity. For

Ni-IMP catalyst, negligible hydrogenation of carbon species was found, which is consistent with its poor catalytic reforming activity. The tendency to form carbon deposits over these spent catalysts is in good agreement with the TG analysis. The difference between Ni-DHT and Ni-GRF TPH profiles reflects that the less stable  $\beta$ -carbon species over Ni-GRF plays a role as the reactive intermediate in the catalytic activity enhancement. Nevertheless, the presence of difficultly removed  $\gamma$ -carbon is associated with the deactivation of Ni-DHT catalyst to some extent.

The textural properties of various spent Ni-containing catalysts were examined by N<sub>2</sub> physisorption. As shown in Fig. 9b, although the BET surface area, the pore volume and the pore size decrease to some extent after the reaction due to the dehydroxylation, carbon deposition, metal sintering and local structure collapse, there still exists the remarkable capillary condensation at the mesoporous range with the corresponding pore diameters of 3.9, 5.1 and 5.1 nm for spent Ni-DHT, Ni-GRF and Ni-IMP, respectively. This proves the good structural stability of the catalysts was retained even under severe reaction conditions.

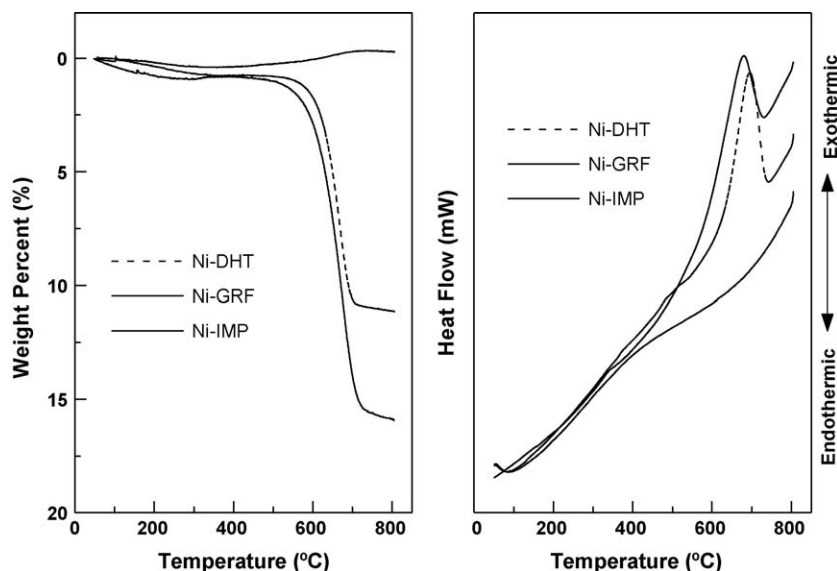


Fig. 8. TG/DTA profiles of spent catalysts after 72 h reaction.

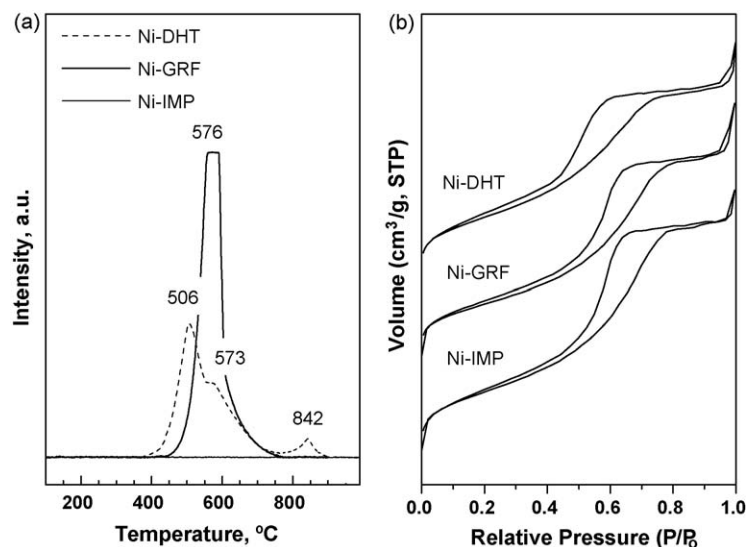


Fig. 9. (a) TGA profiles and (b) N<sub>2</sub> physisorption adsorption isotherms of spent Ni catalyst after 72 h reaction.

No obvious correlation exists between the amount of carbon and the catalytic activity in stability test. Although a negligible amount of carbon is formed on Ni-IMP, both the activity and stability are severely poor. While more carbon was deposited on Ni-DHT and Ni-GRF, both catalysts show good activity and stability, suggesting that higher activity is accompanied by more carbon deposition. Indeed, most of carbonaceous species, both  $\alpha$ -carbon and  $\beta$ -carbon can participate as the reactive intermediates in the production of syngas. For Ni-IMP, the negligible weight loss and the thermal response in TG/DTA analysis imply that the

deactivation of this particular catalyst is not related with carbon formation but due to the significant sintering of nickel particles, which coincides with the lower metal dispersion and larger particle size (see Table 1 and Fig. 10).

To explore the effect of metal particle size, XRD and TEM observations were carried out on the spent catalysts. XRD results (Fig. 7a) show three distinct nickel diffraction peaks at  $2\theta = 44.4^\circ$ ,  $51.9^\circ$  and  $76.6^\circ$ , which are ascribed to Ni(1 1 1), Ni(2 0 0) and Ni(1 1 0), respectively. Only the diffraction peaks corresponding to metallic nickel phase can be observed for all catalysts after

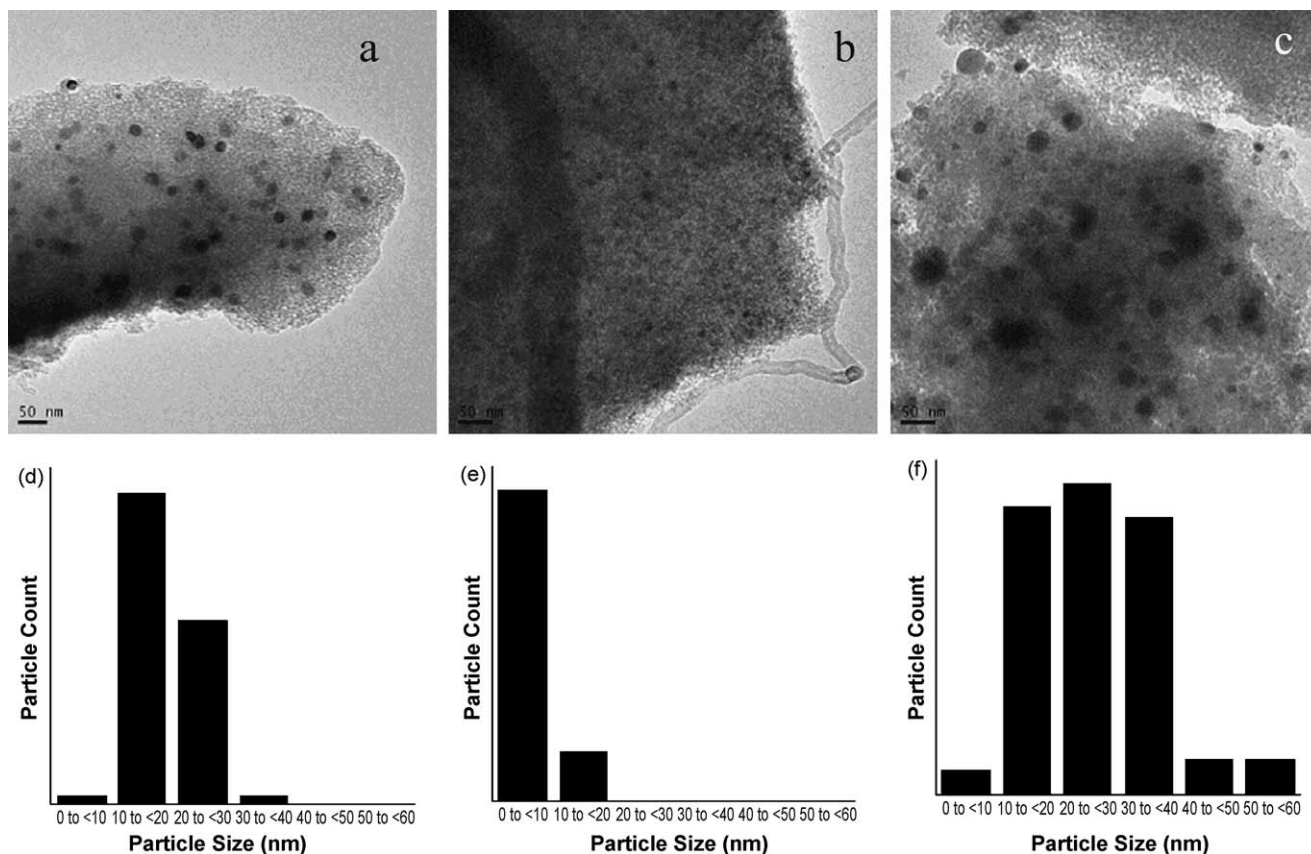


Fig. 10. TEM results for spent catalysts: (1) TEM images for (a) spent Ni-DHT, (b) spent Ni-GRF and (c) spent Ni-IMP, respectively; (2) nickel particle size distributions for (d) spent Ni-DHT, (e) spent Ni-GRF and (f) spent Ni-IMP, respectively.



reactions, implying that all nickel species are in the metallic state and metal aggregation occurs to certain extent during the reaction. The nickel particle size was calculated and summarized in Table 1 according to the Ni(1 1 1) XRD diffraction peak using the Scherrer equation. The TEM images of spend catalyst and their particle size distributions are shown in Fig. 10. The average particle size of nickel is also compiled in Table 1.

The mean particle size of nickel determined by XRD is found to be 17.0, 7.9 and 22.0 nm for Ni-DHT, Ni-GRF and Ni-IMP, respectively. Similar trend of Ni particle size is also observed in TEM determination, namely, 19.2, 8.4, and 26.3 nm for Ni-DHT, Ni-GRF and Ni-IMP samples, respectively. The stabilization of the Co and Ni metallic clusters over mesoporous materials was investigated by Lim et al. using various characterization techniques including CO probe reaction [40]. It was proposed that the anchoring and partial occlusions of metallic clusters on the pore wall of MCM-41 are the main reasons for stabilizing the catalysts against agglomeration. In our studies, it is postulated that similar anchoring effect is responsible for the formation of highly dispersed nickel particles in Ni-DHT and Ni-GRF. Furthermore, for Ni-GRF sample, Ni particles are speculated to be anchored by the terminal Si–O groups rather than the unreduced Ni ions as in Ni-DHT.

Combining the catalytic results and the nickel particle size obtained for various samples, it is manifested that smaller Ni particle is beneficial to the catalytic performance (both activity and stability). Similar trend which correlated particle size and catalytic performance has also been reported [41–45]. The high activity observed on Ni-GRF and Ni-DHT should be caused by the improved dispersion of metal particles under reaction conditions. The large amount of carbon formation can be attributed to the relatively easier decomposition of CH<sub>4</sub> over small nickel particles as demonstrated by Hou et al. in the pulsed-injection surface reaction of methane [43]. The facility of CH<sub>4</sub> decomposition coupled with carbon gasification is beneficial for the formation CO and H<sub>2</sub> via an alternative reaction pathway ( $\text{H}_2\text{O} + \text{C}_{(\text{s})} = \text{CO} + \text{H}_2$ ,  $\Delta H_{298}^\circ = 131 \text{ kcal/mol}$ ) [37]. However, when the decomposition of CH<sub>4</sub> and the Boudouard reaction proceed faster than carbon gasification, accumulation of carbon on the catalyst occurs [37]. As observed in our results, a decrease in Ni particle size has resulted in a larger amount of coke formation over Ni-GRF and Ni-DHT, as mentioned in this section. Although a large amount of carbonaceous species formed over these two catalysts, their catalytic activity and stability are well maintained, especially for the former catalyst. This is most likely due to the low probability of the blocking of the active sites by carbon deposition or the absence of pore-mouth plugging over these catalysts; noticeably, there are more exposed surface active sites over Ni-GRF catalyst.

#### 4. Conclusions

Nickel containing TUD-1 catalysts were prepared by grafting, direct synthesis, and impregnation methods; catalytic properties of these catalysts were probed with carbon dioxide reforming of methane. XRD and TPR results showed that a small amount of NiO aggregates were formed on Ni-DHT and Ni-GRF along with highly dispersed NiO nano-clusters. Although the direct synthesized Ni catalyst performed the best during the catalytic activity test, the grafted catalyst surpassed all other Ni catalysts in the long-term activity and stability evaluation. Despite the presence of a large amount of carbon deposition, Ni-grafted TUD-1 catalyst exhibited high activity and strong resistance against catalyst deactivation due to the presence of more easily accessible Ni active sites and the

nature of the moderate reactivity of surface carbonaceous species. Hence Ni-grafted TUD-1 catalyst can be designated as a superior catalyst candidate for the reforming of methane with carbon dioxide.

#### Acknowledgements

The authors thank AcRF tier 2 (ARC13/07) for providing funding support. The financial support of AcRF tier 1 (RG45/06) is gratefully acknowledged.

#### References

- [1] F. Paraguay-Delgado, R. Garcia-Alamilla, J.A. Lumberreras, E. Cizniga, G. Alonso-Nunez, J. Nanosci. Nanotechnol. 8 (2008) 6406–6413.
- [2] V.V. Shinkarev, A.M. Glushenkov, D.G. Kuvshinov, G.G. Kuvshinov, Appl. Catal. B 85 (2009) 180–191.
- [3] P. Biswas, D. Kunzru, Chem. Eng. J. 136 (2008) 41–49.
- [4] D. Liu, R. Lau, A. Borgna, Y. Yang, Appl. Catal. A 358 (2009) 110–118.
- [5] Y.X. Pan, C.J. Liu, P. Shi, J. Power Sources 176 (2008) 46–53.
- [6] X.L. Zhu, P.P. Huo, Y.P. Zhang, D.G. Cheng, C.J. Liu, Appl. Catal. B 81 (2008) 132–140.
- [7] M. Rezaei, S.M. Alavi, S. Sahebdehfar, P. Bai, X.M. Liu, Z.F. Yan, Appl. Catal. B 77 (2008) 346–354.
- [8] A. Luengnarumitchai, A. Kaengsilalai, Chem. Eng. J. 144 (2008) 96–102.
- [9] V.C.H. Kroll, H.M. Swaan, C. Mirodatos, J. Catal. 161 (1996) 409–422.
- [10] Y.X. Pan, C.J. Liu, L. Cui, Catal. Lett. 123 (2008) 96–101.
- [11] X.L. Zhu, Y.P. Zhang, C.J. Liu, Catal. Lett. 118 (2007) 306–312.
- [12] J.S. Beck, J.C. Vartuli, W.J. Roth, M.E. Leonowicz, C.T. Kresge, K.D. Schmitt, C.T.W. Chu, D.H. Olson, E.W. Sheppard, S.B. McCullen, J.B. Higgins, J.L. Schlenker, J. Am. Chem. Soc. 114 (1992) 10834–10843.
- [13] A. Corma, Chem. Rev. 97 (1997) 2373–2420.
- [14] D. Zhao, J. Feng, Q. Huo, N. Melosh, G.H. Fredrickson, B.F. Chmelka, G.D. Stucky, Science 279 (1998) 548.
- [15] J.C. Jansen, Z. Shan, L. Marchese, W. Zhou, N. Puil, Th. Maschmeyer, Chem. Commun. (2001) 713–714.
- [16] B.Y. Huang, X.J. Li, S.F. Ji, B. Lang, F. Habimana, C.Y. Li, J. Nat. Gas Chem. 17 (2008) 225–231.
- [17] Y.C. Lou, H.C. Wang, Q.H. Zhang, Y. Zhang, J. Catal. 247 (2007) 245–255.
- [18] A. Carrero, J.A. Calles, A.J. Vizcaino, Appl. Catal. A 327 (2007) 82–94.
- [19] G.A. Du, S.Y. Lim, M. Pinsult, C. Wang, F. Fang, L. Pfefferle, G.L. Haller, J. Catal. 253 (2008) 74–90.
- [20] M.L. Zhang, S.L. Ji, L.H. Hu, F.X. Yin, C.Y. Li, H. Liu, Chin. J. Catal. 27 (2006) 777–781.
- [21] K. Wang, X.J. Li, S.F. Ji, S. Sun, D.W. Ding, C.Y. Li, Stud. Surf. Sci. Catal. 167 (2007) 367–372.
- [22] Z.P. Hao, H.Y. Zhu, G.Q. Lu, Appl. Catal. A 242 (2003) 275–286.
- [23] S.B. Wang, H.Y. Zhu, G.Q. Lu, J. Colloid Interface Sci. 204 (1998) 128–134.
- [24] Y.I. Yermakov, Catal. Rev. Sci. Eng. 13 (1976) 77–120.
- [25] G. Du, S. Lim, M. Pinault, C. Wang, F. Fang, L. Pfefferle, G.L. Haller, J. Catal. 253 (2008) 74–90.
- [26] S.M. Rivera-Jiménez, A.J. Hernández-Maldonado, Micropor. Mesopor. Mater. 116 (2008) 246–252.
- [27] C. Aquino, T. Maschmeyer, in: V. Valtchev, S. Mintova, M. Tsapatsis (Eds.), Ordered Porous Solids: Recent Advances and Prospects, Elsevier Science, 2009, pp. 3–30.
- [28] S. Brunauer, P.H. Emmett, E. Teller, J. Am. Chem. Soc. 60 (1938) 309–319.
- [29] E.P. Barrett, L.G. Joyner, P.P. Halenda, J. Am. Chem. Soc. 73 (1951) 373–380.
- [30] M.S. Morey, S. O'Brien, S. Schwarz, G.D. Stucky, Chem. Mater. 12 (2000) 898–911.
- [31] J.M. Rynkowski, T. Paryjczak, M. Lenik, Appl. Catal. A 106 (1993) 73–82.
- [32] S.R. Kirumakki, B.G. Shpeizer, G.V. Sagar, K.V.R. Chary, A. Clearfield, J. Catal. 242 (2006) 319–331.
- [33] M. Montes, C. Penneman De Bosscheyde, B.K. Hodnett, F. Delannay, P. Grange, B. Delmon, Appl. Catal. 12 (1984) 309–330.
- [34] M. Che, Z.X. Cheng, C. Louis, J. Am. Chem. Soc. 117 (1995) 2008–2018.
- [35] B. Pawelec, S. Danyanova, K. Arishtirova, J.L.G. Fierro, L. Petrov, Appl. Catal. A 323 (2007) 188–201.
- [36] S. Shylesh, A.P. Singh, J. Catal. 228 (2004) 333–346.
- [37] M. Haghighi, Z.Q. Sun, J.H. Wu, J. Bromly, H.L. Wee, E. Ng, Y. Wang, D.K. Zhang, Proc. Combust. Inst. 31 (2007) 1983–1990.
- [38] A.E. Galetti, M.F. Gomez, L.A. Arrua, M.C. Abello, Appl. Catal. A 348 (2008) 94–102.
- [39] T. Nozaki, W. Fukui, K. Okazaki, Energy Fuels 22 (2008) 3600–3604.
- [40] S. Lim, C. Wang, Y. Yang, D. Ciuparu, L. Pfefferle, G.L. Haller, Catal. Today 123 (2007) 122–132.
- [41] J.H. Kim, D.J. Suh, T.J. Park, K.L. Kim, Appl. Catal. A 197 (2000) 191–200.
- [42] G.S. Gallego, F. Mondragon, J. Barrault, J.M. Tatibouet, C. Batiot-Dupeyrat, Appl. Catal. A 311 (2006) 164–171.
- [43] Z.Y. Hou, J. Gao, J.Z. Guo, D. Liang, H. Lou, X.M. Zheng, J. Catal. 250 (2007) 331–341.
- [44] J.Z. Guo, Z.Y. Hou, J. Gao, X.M. Zheng, Energy Fuels 22 (2008) 1444–1448.
- [45] Y.H. Wang, H.M. Liu, B.Q. Xu, J. Mol. Catal. A: Chem. 269 (2009) 44–52.